Multimode interferometric sensors on silicon optimized for fully integrated complementary-metal-oxide-semiconductor chemical–biological sensor systems

Jeffrey J. Lillie, Mikkel A. Thomas, Nan-Marie Jokerst,* and Stephen E. Ralph

School of Electrical and Computer Engineering, Georgia Institute of Technology, 791 Atlantic Drive, Atlanta, Georgia 30332-0269

Karla A. Dennis and Clifford L. Henderson

School of Chemical & Biomolecular Engineering, Georgia Institute of Technology, 311 Ferst Drive, N.W., Atlanta, Georgia 30332-0100

Received February 28, 2005; revised July 29, 2005; accepted September 28, 2005; posted October 28, 2005 (Doc. ID 60159)

We demonstrate an integrated evanescent-field multimode Mach–Zehnder interferometric chemical–biological sensor, fabricated on silicon, with sensitivity of parts per 10^9 achieved by modal pattern tracking and analysis. This sensor is fully compatible with the fabrication constraints of the silicon–complementary-metal-oxide-semiconductor (Si-CMOS) process. Furthermore, using the separately measured ellipsometric response together with the mass uptake of agent by the polymer sensing layer, we validate sensor performance via simulation and measure an absolute index sensitivity of 2.5×10^{-6}. We then extend this to a fully integrated chemical–biological sensor by considering the fundamental noise performance of CMOS detectors. We find that relatively short, <5000 μm long, interferometric sensing elements, with modal pattern analysis, allow fully integrated optical sensors on Si-CMOS (assuming a 2.8 μm pixel pitch) with an index sensitivity of $\sim9.2\times10^{-7}$ and a corresponding concentration sensitivity of ~170 parts per 10^9 for methanol in N_2. © 2006 Optical Society of America

OCIS codes: 130.6010, 120.3180.

1. INTRODUCTION

Optical evanescent-wave sensors (EWSs) in various forms have been exploited for highly sensitive chemical–biological sensing. Grating-based EWSs[1] indicate the presence of a target agent through a change in the grating diffraction angle. Surface-plasmon-resonance sensors exploit agent-induced changes in the coupling angle into a surface-plasmon mode.[2] Resonant cavities are also used to enhance photon lifetime, increasing fluorescence in response to a target agent.[3] The intensity change due to an agent-induced shifting of a cavity resonance can also be monitored[4] for high index sensitivity. Another approach, interferometry,[5] utilizes differential phase-based detection for high sensitivity. Recently, reverse-symmetry waveguides employing low-index composite materials are used to increase evanescent penetration into a sensitive upper cladding layer.[6] However, fully integrated EWS systems that exploit one of these methods, and also include sources, detectors, and signal-processing circuitry, remain a challenging but highly desirable goal. We report a compact, easily fabricated, and robust multimode Mach–Zehnder interferometric (MZI) EWS, fabricated on silicon, that can be fully integrated with detection and signal-processing functions on a commercial foundry–fabricated silicon–complementary-metal-oxide-semiconductor (Si-CMOS) circuit. Indeed, we have fabricated these sensors on Si-CMOS circuitry,[7] which includes detector arrays and readout functionality. Furthermore, thin-film lasers that can be precisely transferred onto silicon are also being developed.[8]

The large transverse size of multimode waveguides facilitates coupling and increases the sensing area, yet quantifying and exploiting the complex modal pattern changes are challenging. Furthermore, a practical integrated device is constrained to lengths of a few millimeters, limiting the agent-induced phase change and thus the modal pattern changes. Optimally exploiting modal pattern change is thus key to the deployment of multimode sensors. Here, we report the demonstration and evaluation of multimode interferometric sensors that exploit a simple, but effective, modal image-processing strategy.

One arm of the MZI is sensitized by a chemical sensing layer (SL), in this case a substituted-polynorbornene polymer. The index and thickness changes induced in this SL by an agent are vital to understanding and optimizing the response of EWSs. We have, therefore, developed an efficient method to characterize changes in the index of refraction, extinction coefficient, and layer thickness of the SL, in response to calibrated concentrations of an agent, using a sealed chamber and a high-speed spectroscopic ellipsometer. Simultaneously, agent mass uptake in a separate but identical SL is monitored by a quartz-crystal microbalance (QCM). The mass uptake is linked to the

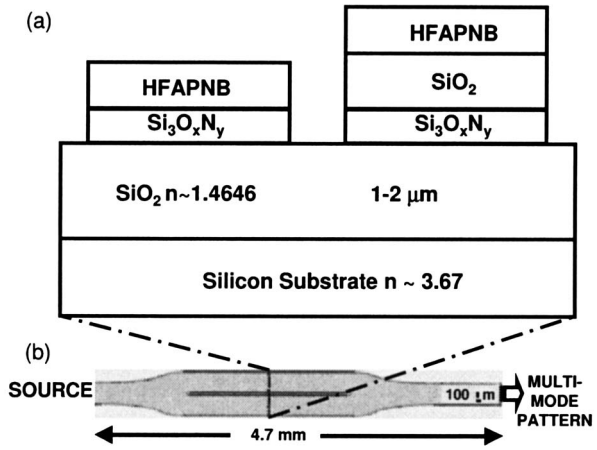

Fig. 1. (a) Cross section of the interferometric sensor. From bottom to top, the waveguide structure consists of a 1–2 μm thick SiO_2 layer and a 0.25 μm thick SiO_xN_y guiding layer ($n_{840\,nm} \sim 1.9223$). On the (left) sensing arm, there is a 0.95 μm thick layer of the polynorbornene polymer, HFAPNB ($n_{840\,nm} \sim 1.4301$), above the guiding layer. On the reference arm, a 1 μm thick SiO_2 layer separates the guiding layer from the HFAPNB layer. (b) Surface relief of the interferometric sensor.

concentration of a vapor phase agent as indicated by a mass flow controller (MFC). This material response data permit device simulation and prediction of its sensitivity to other agents. The temperature dependence of the SL index is also considered in relation to device sensitivity.

The interferometric sensors have been fabricated on silicon and tested using an 830 nm laser, a CCD array, and a hermetic waveguide test chamber. We observe an index sensitivity (for a 1 s integration time) of 2.5×10^{-6} with a corresponding methanol concentration sensitivity of ~450 parts-per-10^9 vapor (ppbv). This index sensitivity is developed by tracking an aggregate normalized power difference of the pixels in the image as the modal pattern shifts owing to index change in the SL. In addition, with the measured response of the polymer sense layer,[9] the corresponding concentration sensitivities for water, benzene, and isopropanol have been set at 15, 30, and 150 ppbv, respectively. The sensitivity is limited by coupling fluctuation in the external coupling of the source laser. We show that the intrinsic noise performance of Si-CMOS detectors allows at least a 5× improvement in sensitivity. Finally, we discuss device sensitivity in terms of the signal-to-noise ratio (SNR) by using a formalism based on a bit error rate.

Chemical or biological EWSs detect a direct or indirect interaction between the evanescent field of a guided mode and a chemical or biological agent. Planar waveguide EWSs typically comprise an optically thin ($<\lambda_0/n_f$), high-index (1.8–2.0) guiding layer sandwiched between a relatively lower-index (1.45) lower cladding layer and a sensitive upper cladding layer; Fig. 1. This upper cladding layer is the SL, since it absorbs or otherwise interacts with the target agent. The thin guiding layer forces much of the evanescent field into the SL while ensuring that the waveguides are single mode perpendicular to the plane of the substrate. Changes in the SL refractive index induce corresponding changes in the effective indices, n_{eff}, of the guided modes, through the slab waveguide boundary-value problem.[10] The changes in propagation and mode field shapes are associated with this change in n_{eff}. With a sensitive geometry, changes in some waveguide parameter (layer thickness or index) strongly affect the modal effective indices. The geometry of the sensing arm [Fig. 1(a)] includes the SL, with an index of refraction, n_{SL}, and a thickness, h_{SL}. Since only the SL is affected by the agent (i.e., the core and lower cladding are not affected), the sensitivity of the effective index of each mode can be written as

$$\Delta n_{eff} = \frac{\partial n_{eff}}{\partial n_{SL}}\,\partial n_{SL} + \frac{\partial n_{eff}}{\partial h_{SL}}\,\partial h_{SL}. \quad (1)$$

Maximizing the sensitivity coefficients, $\partial n_{eff}/\partial n_{SL}$ and $\partial n_{eff}/\partial h_{SL}$, is thus key to sensor performance. Following the approach of Chilwell and Hodgkinson,[11] one can numerically estimate these parameters for multilayer waveguides. The strength of these sensitivity coefficients for the single, vertical transverse-magnetic-like (TM-like) mode, for a range of guiding layer thicknesses, is shown in Fig. 2. TM polarization is chosen because the evanescent field extends further into the SL than for TE polarization. The optimal guiding layer thickness depends on the relative indices and thicknesses of other waveguide layers. If the sense layer index is less than that of the lower cladding (LC), $n_{SL}<n_{LC}$, there is an optimum thickness for the index-sensitivity coefficient. This peak in sensitivity for $n_{SL}<n_{LC}$ can be understood as a redistribution of the electric field. A thick guiding layer ($t_{GL}>0.25$ μm) contains most of the mode field. For thinner guiding layers ($0.14\ \mu m<t_{GL}<0.25\ \mu m$), more mode field is located in the SL and lower cladding. For still thinner guiding layers ($t_{GL}<0.14$ μm), more field is located in the higher-index lower cladding than in the SL, reducing the magnitude of the index-sensitivity coefficient. If $n_{SL}>n_{LC}$, so-called reverse symmetry, the optimum thickness is the thinnest core layer that supports a guided mode. Furthermore, the maximum index-sensitivity coefficient for a higher-index SL is approximately twice that of a lower-index SL.

Although the guiding layer thickness is typically chosen to maximize the coefficients of Eq. (1), a thicker-than-

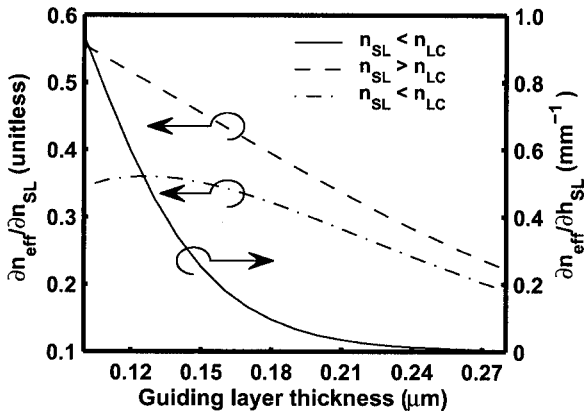

Fig. 2. Sensitivity of the single, TM-like vertical mode effective index, Δn_{eff}, to SL index changes, δn_{SL}, and SL thickness changes, δh_{SL}, for a 0.9 μm thick sense layer. The index sensitivity of a higher-index SL, compared with the lower cladding ($n_{SL}>n_{LC}$), is higher than for a lower-index SL ($n_{SL}<n_{LC}$).

optimum guiding layer may be chosen to ease coupling. Indeed, the devices reported here have a guiding layer thickness of 0.20 μm. This yields an index-sensitivity coefficient, $\partial n_{\mathrm{eff}}/\partial n_{\mathrm{SL}}=0.29$, and a thickness-sensitivity coefficient, $\partial n_{\mathrm{eff}}/\partial h_{\mathrm{SL}}=4.9\times10^{-5}/\mu$m. Using the ellipsometric test, described later, we show that index changes generally affect the modal effective index much more than thickness changes do. For example, when the polymer SL, bis-trifluoromethyl carbinol-substituted polynorbornene (HFAPNB), is subjected to 55 parts-per-10^6 vapor (ppmv) of methanol in N_2, the index change, δn_{SL}, is $\sim3.2\times10^{-4}$, and its thickness change, δh_{SL}, is $\leq1\times10^{-4}$ μm, for a nominally 1 μm thick SL. The effective index shift due to the SL index change, 9×10^{-5}, is at least 10 000$\times$ greater than that due to the SL thickness change, 5×10^{-9}. Since index changes dominate, we neglect thickness changes in subsequent calculations.

As the optical constants and thicknesses of each layer have a thermal dependence, so does n_{eff}. One can reduce temperature effects by ensuring that both interferometer arms have identical optical path lengths. However, this cannot eliminate temperature dependencies. The relative effects of chemical and thermal changes on the optical properties of common polymer and dielectric materials, applied to EWSs, are presented elsewhere.[9] Briefly, the index sensitivity is $-2.4\times10^{-4}/°$C for the polymer, HFAPNB, and $-2.0\times10^{-5}/°$C in SiO_2 and SiO_xN_y. Thus, small temperature variations ($<\pm0.1°$C) may affect the minimum sensitivity as shown later. Fully integrated devices may exploit a reference interferometer, identical to the sensor in every way, except for its insensitivity to the chemical environment. This reference essentially records the changes in the waveguide temperature. The processed output of this reference may be subtracted from that of the chemically sensitive waveguide, yielding a temperature-independent result.

2. EXPERIMENTAL SETUP

A. Fabricated Sensors

One creates the sensor on a chip by first fabricating the necessary complementary-metal-oxide semiconductor (CMOS) circuitry, which includes detector arrays, analog-to-digital converters, and readout circuitry. This is followed by the deposition and definition of the planar waveguide structures. The waveguide process developed and materials used must not impair the functionality of the existing CMOS circuits. The base structure [Fig. 1(a)] includes a 1 μm SiO_2($n_{830\,\mathrm{nm}}\sim1.465$) lower cladding layer that isolates the waveguide from the circuit. It also includes a 0.20 μm high-index ($n_{830\,\mathrm{nm}}\sim1.922$), low-loss SiO_xN_y guiding layer and a 1 μm SiO_2 upper cladding. These materials are deposited using a plasma-enhanced chemical vapor deposition system.[12] The deposition temperature of 200°C does not damage the CMOS circuit. The low-frequency plasma regime is used ($\sim$380 kHz) with an rf power density of $\sim$110 mW/cm^2. On the sensing arm, a 2000 μm$\times$100 μm channel is etched down to the SiO_xN_y guiding layer, and a 1 μm thick layer of the chemically sensitive polymer, HFAPNB ($n_{830\,\mathrm{nm}}\sim1.430$), is spin coated to create the SL.

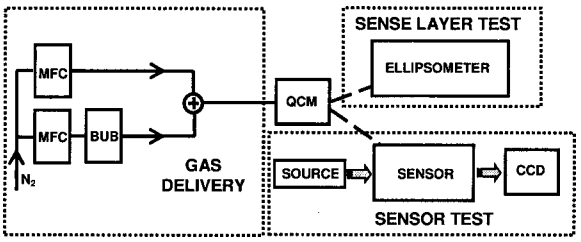

Fig. 3. Experimental setup for measuring the integrated sensor and the SL chemo-optic response. The system delivers 2500 sccm of chemical vapor at concentrations between at 0 and 140 000 ppmv. MFC, mass flow controller; BUB, chemical bubbler; QCM, quartz-crystal microbalance.

Multimode MZI EWSs were fabricated using these materials both on silicon and on a CMOS chip that includes embedded detectors and associated signal-processing circuitry.[13] To access a large-yield Si-CMOS process, the devices reported here are designed to fit into an area of 4.6 mm$\times$4.7 mm, consistent with a standard size of the MOSIS foundary.[14] The MZIs are 4500 μm long and have 100 μm wide waveguides [Fig. 1(b)], with interferometer arms that are 2000 μm in length. These waveguides support nominally 300 modes. The input side of the interferometer is split at a y junction, which has a $\sim$3.3° branching angle and a length of 750 μm. An active sensing arm and a passive reference arm are located immediately after the y junction. On the passive reference arm, an SiO_2 buffer layer prevents interaction between the evanescent field and the sensing material. On the active arm, the large vertical evanescent field extends into the chemically sensitive layer. This target agent interaction alters the SL index. This alters the modal phase differences between each corresponding mode. This altered SL index also results in intermodal coupling. Both phase differences and intermodal coupling modify the composite output modal pattern.

B. Real-Time Optical Constant and Mass-Uptake Measurement of the Sense Layer

Gas delivery and optical characterization systems, Fig. 3, were developed to precisely assess the SL optical response to calibrated concentrations of vapor phase agents. The gas delivery system controls the concentration and flow rate of target agents by mixing the flow of the target agent, controlled by an MFC at 0 to 2 standard cubic centimeters per minute (sccm), with that of a carrier gas, controlled by an MFC at 0 to 2500 sccm. With this system, methanol vapor can be delivered at concentrations between 0 and 1.4×10^5 ppmv with a precision of ±1 ppmv. This gas mixture flows to a custom chamber, mounted on a high-speed, spectroscopic ellipsometer.[15] The wavelength-dependent (300 to 1100 nm) data and their subsequent analysis allow an accurate assessment of the index and thickness changes in the sensing material in response to a range of agent concentrations. As data are acquired at $\sim$0.17 Hz, the materials' transient responses are measured. Also in the flow is a quartz-crystal microbalance (QCM), which measures chemical mass uptake into the SL through the resonant frequency shift of a quartz crystal identically coated with the SL material. This chemical mass uptake is thus precisely linked to its

optical index change. This simultaneous vapor concentration, mass uptake, and optical constant data provide a calibration of the various SL responses and provide accurate physical constants for numerical simulations.

C. Sensor Measurement

The interferometric sensor is located within a separate, hermetic chamber and simulated by the previously described gas delivery system. Light from an 830 nm Fabry–Perot semiconductor laser is coupled into the TM modes of the interferometer. The excitation spot is 10 μm in diameter and is positioned by visually monitoring the scattered light, ensuring that both arms of the interferometer receive half of the coupled power. The output modal pattern is imaged onto a CCD array that captures images at 10 frames/s. These frames are digitally averaged for an effective optical integration time of ~1 s. A long-working-distance objective enables the waveguide facet to be imaged from within the 1.5 in. (1 in.=2.54 cm) wide chamber, but the numerical aperture (0.4) does not capture approximately two thirds of the modes, which exit the waveguide at the steepest angle. Care is taken to ensure stable coupling at the MZI input to minimize coupling-induced modal pattern fluctuations. In the absence of an agent, the total power is stable to ±0.3% over 80 min. We also observe a correlation between power variations and agent concentration. However, we have found that the modal image structure, not total power, is a more sensitive and reliable indicator of chemical concentration, and therefore all images are normalized to constant power. The accurate gas delivery of the chemical agents permits this sensor response to be linked to chemical concentration and, through the ellipsometric measurements, to SL index change. Simultaneously with modal image acquisition, the QCM records the mass uptake of the target agent. These QCM readings provide additional confirmation of the concentration and hence index changes.

3. SIMULATION DETAILS

We use the effective index method together with the ellipsometrically obtained index data to accurately simulate and optimize the sensor structure. The effective index method[10] allows the modal wave vectors of waveguides with two-dimensional cross sections to be estimated through one-dimensional computations. This method accurately represents waveguides that are transversely wide (i.e., wider than 100λ) in at least one dimension.

The vertical effective indices are calculated using a multilayer formulation, and the horizontal effective indices are then numerically calculated using the two-dimensional beam propagation method[16] (BPM). The BPM is used to numerically include the effects of the MZI y junctions and associated intermodal coupling. Because the guiding layer is thin (i.e., $<\lambda/2$), with a high index contrast (i.e., ~0.45), predominantly a single vertical TM-like mode is excited. The two main vertical waveguide structures include the reference arm [Fig. 1(a), right] and the sensing arm [Fig. 1(a), left]. The sensing arm TM-like effective indices are calculated under various states of chemical absorption, and these changing effective indices are the index input to a transverse electric (TE) BPM simulation. For each state of chemical absorption, the incident Gaussian illumination is numerically propagated through the interferometer, including the sensing region. The series of multimode patterns that are produced represent the sensor action during progressive chemical absorption. Variations in fabricated waveguide indices and dimensions and variations in illumination preclude a one-to-one comparison between experimental and numerical modal patterns. However, it is expected that the changes in patterns behave in a statistically similar manner for equivalent chemical concentrations or SL index changes.

4. RESULTS

A. Real-Time Optical Constant and Mass-Uptake Evaluation of the Sense Layer

The dynamic optical response of the polymer, HFAPNB, to a range of methanol vapor concentrations has been determined using the previously described gas delivery and optical characterization systems. Figure 4(a) depicts the index response for a change from negligible to 140 ppmv of methanol in N_2. The corresponding mass uptake [Fig. 4(b)] is measured via QCM frequency shift. Accurate mass flow control devices link the vapor concentration of agent to mass uptake and index change in the SL. The test procedure begins with an N_2 purge, continues as a chemical-laden vapor stream is introduced into the chamber, and concludes with another N_2 purge. Figure 4 shows multiple cycles of this procedure. The data shown begin while the chemical is in the chamber, indicated by increased index [Fig. 4(a)] and mass uptake [Fig. 4(b)]. For the sense material, HFAPNB, we observe an index change that scales linearly with concentration change and mass uptake of methanol for concentrations between 0 and 1000 ppmv. Specifically, $\Delta n_{SL} \sim 5.6\times10^{-6}$(1/ppmv), and $\Delta n_{SL} \sim 5.4\times10^{3}$ (cm^2/g), where $\Delta m/A$(g/cm^2) is the mass uptake per unit area of the polymer film. The response is not linear near saturated flows, i.e., for concentration changes greater than 8000 ppmv.

We note a baseline drift in the index response, while the baseline in the mass uptake is essentially constant.

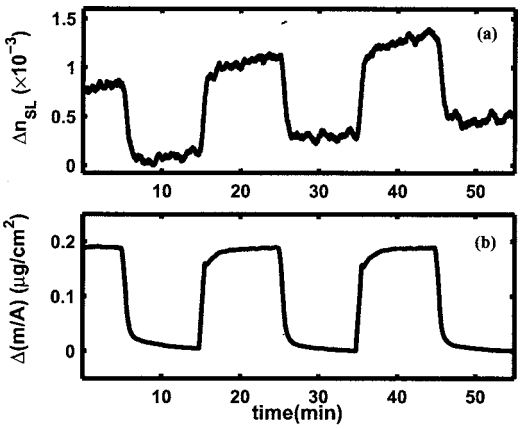

Fig. 4. (a) Ellipsometric response, Δn_{SL}, of the chemically sensitive polymer, HFAPNB, to 140 ppmv of methanol vapor. (b) The corresponding QCM response. For low concentrations, Δn_{SL} responds linearly with mass uptake and concentration with $\Delta n_{SL} \sim 5.4\times10^{3}$(cm^2/g) and $\Delta n_{SL} \sim 5.6\times10^{-6}$(1/ppmv).

These observations are consistent with polymer densification. Since the mass uptake is constant, the index drift is not a result of chemical accumulation in the polymer. Further, the baseline polymer thickness (not shown) also decreases, supporting densification. In fact, Drozdov[17] explains theoretically the experimental observation that both compressive and tensile stresses cause densification of glassy polymers. The observed cyclic increase and decrease in thickness that is induced in HFAPNB by repeated cycling between chemical atmosphere and N_2 cause tensile stresses in the polymer. Thus, the baseline drift in the index data is likely caused by polymer densification.

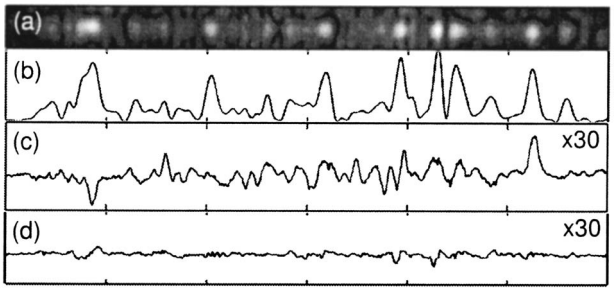

Fig. 5. Representative multimode patterns. (a) Captured CCD image. (b) Corresponding intensity profile. (c) Pixel power difference pattern for 37 ppmv CH_3OH. This difference in the patterns indicates detection. (d) Pixel power difference pattern with no applied chemical. All patterns are 100 μm wide.

B. Sensor Measurement

Modal patterns are digitally sampled at 10 Hz and integrated to give an effective bandwidth of 1 Hz by using a 640×480 element CCD array. A representative multimode image is shown in Fig. 5(a). Figure 5(b) shows the corresponding one-dimensional (integrated vertically) intensity. The difference between intensity patterns at 0 and 37 ppmv methanol in N_2 is shown in Fig. 5(c). In contrast, the variation or noise corresponding to a steady, near-zero concentration is shown in Fig. 5(d). The goal is to accurately identify significant modal pattern changes as in Fig. 5(c) in the presence of the modal pattern noise shown in Fig. 5(d). The difference between the signal in Fig. 5(c) and the noise in Fig. 5(d) illustrates that the sensing of tens of parts per 10^6 of methanol in vapor is readily achievable. Optimal pattern interpretation, i.e., signal processing to optimize the SNR, can significantly improve sensitivity.

Figure 6 shows a comparison between simulated and measured modal difference patterns for a methanol vapor concentration change of 35 ppmv. The modal difference pattern at time t can be written as $P(t,j)-P(0,j)\forall\, j$, where $P(t,j)$ is the power of pixel j at time t (the pixel signal is actually an integrated power). Although the overall magnitudes of the deviations are similar for simulated and experimental modal patterns, the shape is sensitive to the details of the fabricated structure, the illumination, and the detection system. Here, the experimental pattern has a slightly smaller standard deviation. The simulated patterns were created using the BPM and then integrated spatially to match the effective experimental resolution. Although the output resolutions are similar, the exact illumination conditions may be different, exciting different numbers of modes under the SL and causing different modal pattern repetition periods. This would account for the difference in standard deviations between simulated and measured patterns. However, as discussed below, a method of quantifying the deviation is sufficient to calibrate the sensor response.

The effective experimental pixel pitch is estimated at 1.4 μm, which is determined by the experimental optics and not the CCD array. The long-working-distance objective has an acceptance half-angle of 24°, insufficient to capture some higher-order modes. Unfortunately, the higher-order transverse modes have a longer effective path length under the SL and are inherently more sensitive. This limitation can be overcome by different outcoupling methods, such as a grating or a larger numerical-aperture objective.

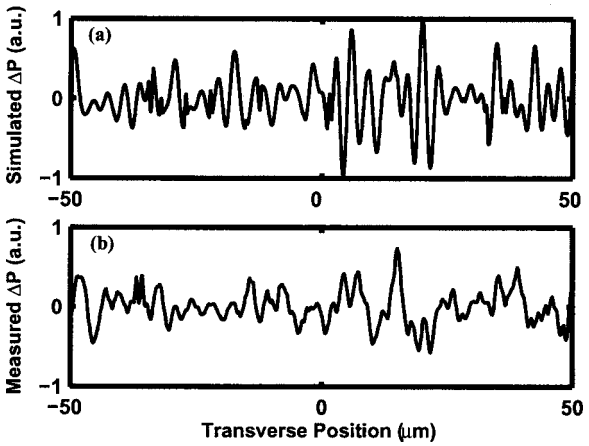

Fig. 6. (a) Simulated and (b) measured multimode difference patterns, which show the pattern changes after a methanol vapor concentration change of 35 ppmv. This corresponds to a SL index change of 2×10^{-4}.

Optimizing the sensitivity requires a quantitative assessment of modal pattern changes. This pattern assessment requires an appropriate figure of merit (FOM) to reliably and quantitatively detect an agent-induced index change in the presence of noise. We note that the modal pattern from each sensor, and hence each data set, varies owing to subtle changes in coupling and the associated changes in mode intensity in the multimode waveguide. Regardless of the particular multimode pattern, the FOM should produce a largely identical response for a given concentration change. Here, we report the performance of combined pixel power tracking (CPPT), since it is a simple, sensitive, and robust FOM for quantifying the multimode pattern changes.

Specifically, a useful FOM is based on the response of many pixels and allows for pixels with different starting powers and response magnitudes. In addition, it must account for pixels that respond with an increase or decrease in power to the chemical. For example, Fig. 7 shows the raw pixel power responses of three representative pixels. For the highest-power pixel, a concentration change from 54 to 75 ppmv produces a disproportionate (no) change

compared with the last three concentration changes (30, 15, and 8 ppmv), which produce an easily identifiable and proportional power change. This lack of change is due to the complex interaction of the waveguide modes. Further, the middle-power pixel increases power in response to the chemical, whereas the other pixels decrease. Finally, this FOM should produce the greatest SNR in response to the chemical concentration. And, it must be quantifiably, preferably linearly, related to the chemical concentration change. We show that CPPT involves the combined power changes of all pixels within the modal pattern image and thus meets these criteria.

Optimal combinations of the observations of a set of sensors, each observing an event with a different SNR, have been studied extensively.[18] For this sensor, many pixels record a slightly different version of the sense event with a different SNR. The optimal combination of pixels should maximize the SNR and maintain a quantifiable relationship with the SL index and hence chemical concentration. We assume that the noise of each pixel is uncorrelated and has Gaussian statistics. Experimentally, we find limited correlation among pixels due primarily to the modal structure of the image. We look for the optimal weights, w_j, to assign to the changes occurring in each pixel in response to the chemical. We define pixel power changes as

$$\Delta P(t,j) \equiv |P(t,j) - \langle P(0,j)\rangle_{1\ \mathrm{min}}|, \tag{2}$$

where $P(t,j)$ is the power of pixel j at time t and $\langle P(0,j)\rangle_{1\ \mathrm{min}}$ represents the mean power of a pixel over a reference minute of the measurement (during which time we assume there is no chemical). We form a weighted combination of the responses of N pixels,

$$\Delta P_{wt}(t) = \sum_{j=1}^{N} w_j \Delta P(t,j). \tag{3}$$

By maximizing the joint SNR, we find that the optimal combination is

$$\Delta P_{wt}(t) = \sum_{j=1}^{N} \frac{\Delta P(t,j)}{\sigma_j^2} \Delta P(t,j), \tag{4}$$

where σ_j^2 is the variance in the jth pixel measured over the same reference minute as $\langle P(0,j)\rangle_{1\ \mathrm{min}}$. Brennan[18] suggests these same weights when evaluating maximal-ratio diversity for fading multipath detection of radio transmissions. To maintain linearity in ΔP, which is proportional to index change, we take the square root of this quantity. We therefore define our FOM of modal pattern change, S, as follows:

$$S(t) \equiv \left[\sum_{j=1}^{N} \frac{(\Delta P)^2(t,j)}{\sigma_j^2} \right]^{1/2}. \tag{5}$$

This quantity is simply the root-mean-square SNR of all pixels. This practical, simple measure can easily be implemented using standard CMOS technology, allowing an integrated device with real-time modal pattern processing. Furthermore, the reference parameters, $\langle P(0,j)\rangle_{1\ \mathrm{min}}$ and σ_j^2, can be reassessed at any time, allowing S to represent the change in concentration from the reference time. This reassessment also reduces the long-term drift that is often present in actual sensor systems.

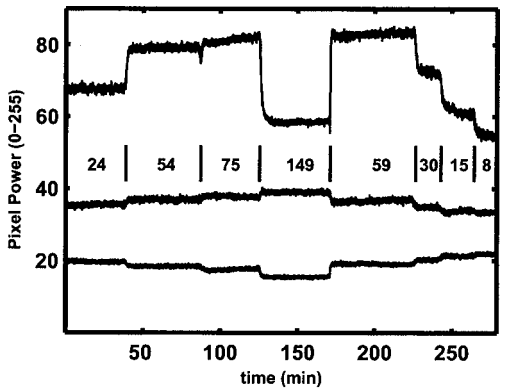

Fig. 7. Magnitude and direction of response vary considerably among three representative pixels as the methanol vapor concentration changes between 24, 54, 75, 149, 59, 30, 15, and 8 ppmv.

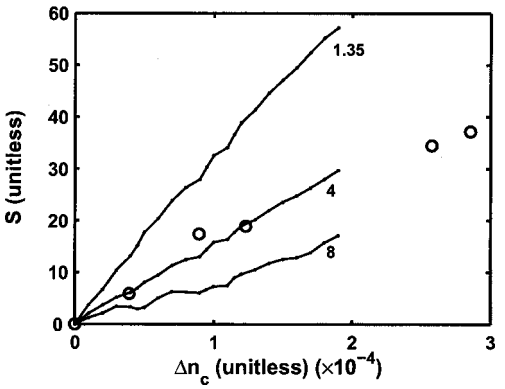

Fig. 8. Simulated (curves) and experimental (circles) sensor responses as measured by the S FOM to an increase in the sense layer index, establishing a direct link between the FOM and the SL index change. Simulated response is shown for pixels with 1.35, 4, and 8 μm pitches; experimental response corresponds to a 1.35 μm pixel pitch.

Figure 8 shows the change in S for a range of SL index changes, Δn_c near 10^{-4}, for both simulated and measured data, and shows that the FOM is proportional to index change. The simulated responses are calculated for three distinct spatial resolutions of the modal pattern corresponding to pitches of 1.35, 4, and 8 μm. The highest sensitivity is achieved with the highest spatial resolution. The measured modal patterns have a spatial resolution corresponding to a pitch of 1.35 μm. The simulated pixels are assumed to have the same relationship between noise variance and pixel power as measured experimentally. We find that the simulation produces a response that is three times greater than the measured response. The apparent higher sensitivity of the simulation can again be explained by the numerical aperture of the experimental optics. However, in the fully integrated system, significantly more modes do impinge on the evanescently or grating-coupled detectors, and the pattern resolution is limited only by pixel pitch.

Like many multimode devices, the output image is periodic in Δn_c, and the FOM is also periodic. However, the period is such that for small Δn_c (5×10^{-4}), the response

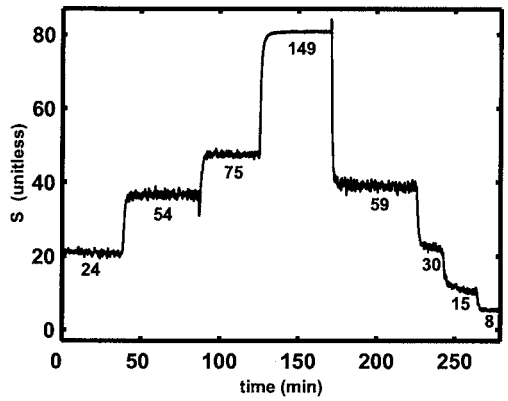

Fig. 9. Aggregate response of all pixels, as quantified by the modal pattern FOM, S. Same concentration changes as in Fig. 7.

is approximately linear as shown in Fig. 8. In fact, the experimental response (circles) is also approximately linear with a slope of ~ 0.73/ppmv. However, at high Δn_c ($>5 \times 10^{-4}$), not shown, the sinusoidal behavior is observed. One can retain the high sensitivity in the linear regime by resetting the reference parameters in real time. Furthermore, multiple reference parameters can be acquired and used to unambiguously identify the index change. Alternately, interferometers with different sensitivities to the agent could be added to the system to modify the index period and thus the dynamic range.

Figure 9 shows the response of the sensor interpreted by the CPPT FOM, S. It has a defined response at each chemical vapor concentration level including the lowest, at 8 ppmv of methanol vapor. The response is notably improved from that of individual pixels (Fig. 7). For concentrations less than 80 ppmv, it is linear with concentration. At higher concentrations (149 ppmv), a slight deviation from linearity in the combined response is observed, consistent with a cyclic response of the multimode pattern. We note that the noise appears to vary with concentration in Fig. 9; however, we have traced the source of this noise, using mass-uptake data (not shown), to the (MFCs), which digitally adjust the flow to maintain the flow rate. The MFC manifold produces the smallest concentration fluctuations at the 149 ppmv level, consistent with flow-rate-dependent fluctuations. At these concentrations, the noise is dominated by other noise sources and not the MFCs. Therefore, we can estimate the minimum sensitivity as limited by the optical noise of the experimental setup. Choosing a minimum sensitivity corresponding to 3σ, where σ is the standard deviation in the signal at 149 ppmv, we see that the results of Fig. 9 demonstrate a sensitivity of 450 ppbv for methanol in N_2.

5. MINIMUM DETECTABLE CONCENTRATION–INDEX CHANGE

We now discuss the implications of a sensitivity limit based on the SNR and extrapolate the demonstrated sensitivities to a fully integrated Si-CMOS-based sensor. The criteria used to compare sensing ability vary considerably in the literature. Schneider *et al.*[19] use a detection limit based on a 10% change in signal intensity. Others use the SNR (SNR=intensity change/σ) as the basis for a detection limit. For example, both Luff *et al.*[20] and Brandenburg *et al.*[21] report a 3σ detection threshold. Although their approach is specific to biological agent detection, Blair and Chen[3] specify a 2σ detection limit. Although environmental fluctuations may be large, it is still useful to specify sensitivity in terms of inherent sensor system noise.

Here, we discuss the basis for these sensitivity estimates and suggest a common comparison standard. We use a methodology similar to the bit error rate formalism, the standard performance measure for communication channels. Simply, the sensitivity is the minimum detectable change (MDC) in sensor output. The MDC is based on the probability of error in the measurement, when changing between two states. The simplest change is between the no-chemical (NC) State and the state of the minimum detectable amount of chemical (C); however, this equally applies in changing between one concentration and another. This is the resolution of the detection system. This error probability is given by

$$p_E = p(\mathrm{NC})p(\mathrm{C}|\mathrm{NC}) + p(\mathrm{C})p(\mathrm{NC}|\mathrm{C}), \tag{6}$$

where $p(\mathrm{NC})$ is the probability of no chemical being present, $p(\mathrm{C}|\mathrm{NC})$ is the probability of indicating a chemical when none is present, $p(\mathrm{C})$ is the probability of having a chemical present, and $p(\mathrm{NC}|\mathrm{C})$ is the probability of not indicating when a chemical is present. The quantities, $p(\mathrm{NC})$ and $p(\mathrm{C})$ are the fraction of time the sensor is in either state. For sensors, a chemical is not present a majority of the time. That is, $p(\mathrm{C}) \ll p(\mathrm{NC})$, resulting in $p_E \sim p(\mathrm{C}|\mathrm{NC})$. In other words, it is mainly the noise distribution when a chemical is not present that determines the total probability of error. However, both the false-positive probability and the false-negative probability are important sensor metrics. Therefore, since $p(\mathrm{NC})$ and $p(\mathrm{C})$ are not known *a priori*, we evaluate $p(\mathrm{C}|\mathrm{NC})$ and $p(\mathrm{NC}|\mathrm{C})$.

The experimental sensor system is dominated by multiplicative noise sources, primarily from optical source intensity and coupling fluctuations and associated image spatial jitter. In addition, these noise sources are uncorrelated, allowing their variances to be added. We find, experimentally, that the combined noise sources have approximately Gaussian characteristics.

In optical sensing, the limit of detection is usually specified by a single parameter, generally 3σ. However, in practice, we should distinguish between the detection threshold and the MDC. If the sensor output exceeds the threshold, a chemical is detected. On the other hand, the MDC is the minimum concentration that can be detected with a specified accuracy. Specifying the MDC at the 3σ level usually requires a threshold lower than 3σ. In general, therefore, both $p(\mathrm{C}|\mathrm{NC})$ and $p(\mathrm{NC}|\mathrm{C})$ are required to choose the MDC and the threshold. When one is minimizing the total probability of error, p_E, and in the limit of $P(\mathrm{C}) \ll P(\mathrm{NC})$, these values are equal. However, in this case, when the sensor is exposed to the MDC, $p(\mathrm{NC}|\mathrm{C}) = 0.5$. That is, the false-negative probability is 50%.

Maintaining an error, $P(\mathrm{NC}|\mathrm{C})$ of 0.1% when a chemical is present requires a threshold of 3σ below the MDC. To maintain this error regardless of chemical state, the threshold must also be set at 3σ above the mean level in

the no-chemical state. This requires that the MDC be 6σ and the threshold be 3σ above the mean level in the no-chemical state (assuming that the noise is independent of the mean signal). Therefore, the 3σ level may not literally represent the minimum detectable concentration in practice. Lastly, we note that Gaussian noise (σ) is reduced with longer integration times, τ. Specifically, the MDC $\propto 1/\sqrt{\tau}$ and is correctly specified in the context of integration time.

Having noted these issues, we choose the minimum detectable index change (minimum detectable concentration change) [MDIC (MDCC)] as the index (concentration) at which the signal changes by 3σ for a 1 Hz bandwidth. On the basis of this formalism, the sensor output (Fig. 9) has an MDIC of $\sim 2.5\times 10^{-6}$. The corresponding MDCC (for methanol vapor) is 450 ppbv. This index sensitivity compares favorably with that of a recent surface-plasmon-based biosensor[2] with a 3σ MDIC of 3.6×10^{-6}. Dostalek *et al.*[2] describe their index sensitivity as 1.2×10^{-6}, but this is the 1σ MDIC.

A. Noise Considerations

We assess the intrinsic system noise and thereby determine the best possible sensitivity. The noise arises from source fluctuations, shot noise, read noise, and noise associated with dark current. Although source fluctuations are often quantified in terms of relative intensity noise,[22] RIN the integration time of sensors requires that the source be quantified in terms of low-frequency fluctuations, i.e., drift. As a fully integrated sensor will include a feedback-stabilized laser, and, as all images are normalized to constant intensity, these fluctuations are negligible. CMOS detectors accumulate photogenerated electrons in a capacitive structure, termed a well. The number of photogenerated electrons, N, is proportional to the optical power, P. Shot-noise variance, which is due to the random arrival time of photons, scales as the mean number of captured photoelectrons.[23] Read noise, which is specified per read event, can be reduced by using a larger well size. The read-noise variance of a typical CMOS array,[24] is $185^2(e^-)^2$. For the same CMOS array at 25°C, and for a 1 s total collection time, the dark-current shot-noise variance is about $135^2(e^-)^2$. Thus, for a well size of $2.125\times 10^6(e^-)$, and sufficient intensities, a fully integrated sensor system is shot-noise limited. However, for pixels with low intensities, read noise and dark-current noise also contribute to the total noise.

Figure 10 depicts the observed noise performance of the experimentally demonstrated sensor (triangles) and the estimated noise performance of a fully integrated sensor (dashed curve) that is limited by fundamental noise sources. The noise level of the demonstrated sensor is higher than that of the fully integrated sensor, which is set by shot noise, read noise, and dark-current noise. The measured noise is not purely additive but is functionally related to intensity. The linear behavior of the measured sensor noise at higher intensities is consistent with signal fluctuation caused by variations in positioning equipment. As this fluctuation will be removed in a fully integrated sensor, we estimate the ultimate sensitivity by considering only the intrinsic noise of the system. When compared with the experimentally measured noise, a reduction in pixel standard deviation (σ) of $\sim 5\times$ and a corresponding reduction in MDIC are possible.

B. Additional Factors and Ultimate Sensitivity

Two additional factors affect the ultimate sensitivity of the fully integrated CMOS sensor: the pixel size and the guiding layer thickness. The pixel size determines the spatial integration of the multimode pattern. In a fully integrated device, the CMOS array may be evanescently or grating coupled. The experimentally measured system, however, includes imaging optics that magnify the multimode pattern incident on the CCD array. The effective resolution experimentally, 1.4 μm, is limited not by the actual camera pixel pitch but by the numerical aperture of this imaging system. Simulated results (Fig. 11) show the sensitivity variation with spatial bandwidth for our 100 μm waveguides. Commercial Si-CMOS detector ar-

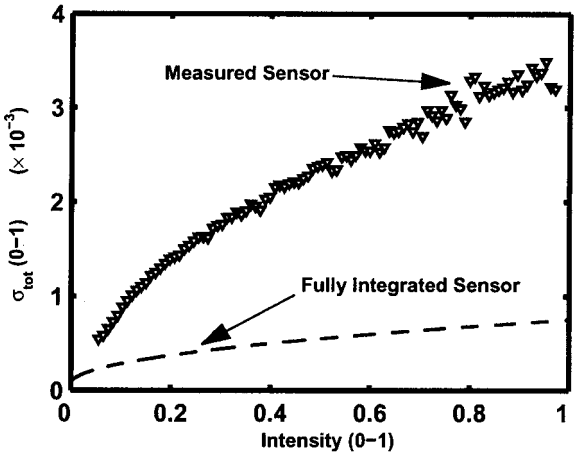

Fig. 10. Comparison between the standard deviation, σ, and the intensity, I, of the measured sensor system (triangles) and the standard deviation estimated for a fully integrated sensor limited by fundamental noise sources (dashed curve), essentially shot noise. This represents a 4–6$\times$ reduction in the noise.

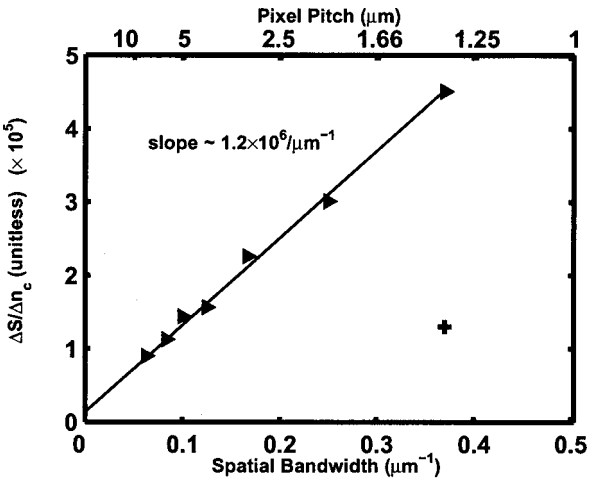

Fig. 11. Simulated data (triangles) showing the effect of spatial resolution in the detected multimode pattern on device sensitivity. An increase in pixel pitch from 1.35 to 2.8 μm reduces sensitivity by $\sim 2.1\times$. Experimental sensitivity (about one third of simulated data at the same spatial bandwidth) is indicated by the cross.

rays are available with a pixel pitch of 2.8 μm.[25] Using an array with this pitch reduces sensitivity by 2.1×.

We can improve the sensitivity by increasing the evanescent field within the sensing layer and thereby the index-sensitivity coefficient, $\partial n_{\mathrm{eff}}/\partial n_{\mathrm{SL}}$. Thinning the current guiding layer thickness from 0.20 μm to the optimal thickness of ~0.13 μm improves sensitivity by 20%. This improvement requires an input grating coupler for practical implementation. These two factors (assuming 2.8 μm pitch) create a net sensitivity reduction of 1.8×. Thus by optimizing guiding layer thickness, accounting for pixel size, and operating in the shot-noise limit, we estimate that the MDIC $\simeq 9.2\times10^{-7}$. This corresponds to a methanol vapor concentration of 170 ppbv.

Having established its index sensitivity, we now infer the response of the sensor to other agents. We have determined the optical response of HFAPNB to isopropanol, benzene, and water by using the described ellipsometric techniques.[9] The index response of HFAPNB to isopropyl alcohol is 33× stronger than that for methanol, the response to benzene is 15× stronger, and the response to water is 3× greater at a given concentration. Thus, the sensitivities of the experimentally measured sensor to isopropanol, benzene, and water are 15, 30, and 150 ppbv, respectively. Extending this to an optimized integrated sensor yields sensitivities for isopropanol, benzene, and water of 6, 12, and 57 ppbv respectively.

We have described an interferometric waveguide sensor platform that is highly sensitive to SL index changes. With HFAPNB as the SL, the sensor is sensitive to methanol vapor, isopropanol, benzene, and water (when introduced independently). However, the underlying sensor platform responds to index changes in any of its optical layers, although this occurs predominantly in the SL material. Both chemical and thermal interactions can create these index changes and potentially interfere with target agent detection.

Further sensor design considers polymer–chemical interactions. If mixtures of chemicals are introduced, the index response depends on the composite index response of the SL. All chemicals present, including the target agent and other environmental chemicals, affect this response. These other environmental chemicals (including water vapor) can obscure the target agent. A selective sensor identifies the target agent in the presence of these obscuring substances. Two methods to develop a selective sensor using the described platform are suggested for future consideration.

The simpler method uses a natural or engineered SL material that is chemically / or physically tailored or both to detect a particular agent. This material could facilitate a chemical reaction that requires the target agent. It could also have some physical shape or size that matches that of the target agent. The index response to the target agent for this kind of SL should be much greater than to other environmental chemicals. This SL would simply replace the HFAPNB SL on the sensor platform. Another method, which does not require materials with specific properties, uses an array of sensors, identical in every way except that they have different polymer SLs. Dennis shows that the different rates of uptake of chemicals into these polymers can be used to differentiate quantitatively the elements of a mixture (including water vapor) of chemical agents.[26]

Further, as specified earlier, the SL index thermal sensitivity is $-2.4\times10^{-4}/°\mathrm{C}$. Limiting the temperature dependence to maintain the MDIC requires that the temperature be held constant to within ±0.004°C. Thus, in the absence of isothermal conditions, a reference sensor must be used to counter this temperature sensitivity.

6. CONCLUSION

In conclusion, we have demonstrated a multimode interferometric chemical sensor on silicon that is fully compatible with the fabrication constraints of Si-CMOS circuitry. The changing modal patterns have been processed using a simple, but effective, modal image-processing strategy, which produces an optimal, robust sensing metric. A technique to measure the material optical response to various target agents has also been demonstrated, permitting device simulation and prediction of device sensitivity to these agents. An error probability formalism was used to define the device sensitivity, the minimum detectable change. The minimum detectable index change of the demonstrated device (for a 1 Hz bandwidth) is 2.5×10^{-6}. The corresponding minimum detectable concentration change for methanol vapor absorbed into HFAPNB is 450 ppbv. The intrinsic noise performance of a fully integrated sensor on Si-CMOS suggests that the attainable minimum detectable index change is $\simeq 9.2\times10^{-7}$. The demonstrated techniques and performance enable the creation of intelligent, adaptable, fully integrated sensor systems.

ACKNOWLEDGMENTS

The authors thank Kasyapa Balemarthy for discussions about SNR optimization. This work is supported in part by the Defense Advanced Research Projects Agency through the University Opto-centers Optical Chemical and Biological Sensors Program.

Stephen Ralph, may be reached by phone at 404-894-5168 or by e-mail at stephen.ralph@ece.gatech.edu.

*Present address, Department of Electrical and Computer Engineering, Duke University, Durham, North Carolina 27708.

REFERENCES

1. W. Challener, J. Edwards, R. McGowan, J. Skorjanec, and Z. Yang, "A multilayer grating-based evanescent wave sensing technique," Sens. Actuators B **71**, 42–46 (2000).
2. J. Dostalek, J. Styroky, J. Homola, E. Brynda, M. Skalsky, P. Nekvindova, J. Spirkova, J. Skvor, and J. Schrofel, "Surface plasmon resonance biosensor based on integrated optical waveguide," Sens. Actuators B **76**, 8–12 (2001).
3. S. Blair and Y. Chen, "Resonant-enhanced evanescent-wave fluourescence biosensing with cylindrical optical cavities," Appl. Opt. **40**, 570–582 (2001).
4. E. Krioukov, J. Greve, and C. Otto, "Performance of integrated optical microcavities for refractive index and fluorescence sensing," Sens. Actuators B **90**, 58–67 (2003).
5. N. F. Hartman, "Integrated optic interferometric sensor," U. S. patent 5623561 (April 22, 1997).
6. R. Horvath, H. Pederson, N. Skivesen, D. Selmeczi, and N. Larsen, "Monitoring of living cell attachment and

spreading using reverse symmetry waveguide sensing," Appl. Phys. Lett. **86**, 071101 (2005).
7. D. Kim, M. Thomas, M. Brooke, and N. Jokerst, "Integration of Si-CMOS embedded photo detector array and mixed signal processing system with embedded optical waveguide input," in *Semiconductor Photodetectors*, K. Linden and E. Dereniak, eds., Proc. SPIE, **5353**, 20–28 (2004).
8. H. Kuo, S. Gho, J. Hall, and N. Jokerst, "Heterogeneous integration of InP/InGaAsP MQW thin film edge emitting lasers and polymer waveguides," in *2004 Proceedings, 54th Electronic Components and Technology Conference*, Part 2 (IEEE, 2004), Vol. 2, pp. 1537–1541.
9. J. Lillie, K. Dennis, C. Henderson, and S. Ralph, of Georgia Institute of Technology, 777 Atlantic Drive N.W., Atlanta, Ga. 30332-0250, are preparing a manuscript to be called "Polymers as 'sensing layers' for evanescent wave sensors."
10. C. R. Pollock, *Fundamentals of Optoelectronics*, 1st ed. (Irwin, 1995).
11. J. Chilwell and I. Hodgkinson, "Thin-films field-transfer matrix theory of planar multilayer waveguides and reflection from prism-loaded waveguides," J. Opt. Soc. Am. A **1**, 742–753 (1984).
12. A. Chambers, D. Stephens, J. Pink, K. Robb, T. Thomas, E. Hinds, and R. Gunn, "Improved deposition rates and uniformity of silica-based films deposited by PECVD on 200 mm substrates," Adv. Electroni. Manuf. Technol. (www.vertilog.com) 1, 1–4 (2004).
13. M. Thomas, J. Lillie, D. Kim, S. Ralph, M. Brooke, K. Dennis, B. Comeau, C. Henderson, and N. Jokerst, "An interferometric sensor for integration with Si CMOS circuitry, 'Sensor-on-a-Chip'," in *Conference on Lasers and Electro-optics/International Quantum Electronics Conference and PhAST Technical Digest on CD-ROM*, TuG6 (The Optical Society of America, Washington D.C., 2004).
14. MOSIS website, "Description of AMIS processes," http://www.mosis.org/products/fab/vendors/amis/ (2005).
15. B. Johs, J. Hale, N. Ianno, C. Herzinger, T. Tiwald, and J. Woollam, "Recent developments in spectroscopic ellipsometry for *in situ* applications," in *Optical metrology Roadmap for the Semiconductor, Optical, and Data Storage Industries II*, A. Duparre and B. Singh, eds., Proc. SPIE **4449**, 41–57 (2001).
16. D. Yevick, "A guide to electric field propagation techniques for guided wave optics," Opt. Quantum Electron. **26**, 185–197 (1994).
17. A. Drozdov, "A model for mechanically induced densification of glassy polymers," J. Appl. Mech. **66**, 702–708 (1999).
18. D. Brennan, "Linear diversity combining techniques," Proc. IEEE **91**, 331–356 (2003).
19. B. Schneider, J. Edwards, and N. Hartman, "Hartman interferometer: versatile integrated optic sensor for label-free, real-time quantification of nucleic acids, proteins, and pathogens," Clin. Chem. **43**, 1757–1763 (1997).
20. B. Luff, J. Wilkinson, J. Piehler, U. Hollenach, J. Ingenhoff, and N. Fabricius, "Integrated optical Mach–Zehnder biosensor," J. Lightwave Technol. **16**, 583–591 (1998).
21. A. Brandenburg, R. Krauter, C. Kunzel, M. Stefan, and H. Schulte, "Interferometric sensor for detection of surface-bound bioreactions," Appl. Opt. **39**, 6396–6405 (2000).
22. K. Lau and A. Yariv, "Ultra-high speed semiconductor lasers," IEEE J. Quantum Electron. **21**, 121–138 (1985).
23. P. Magnan, "Detection of visible photons in CCD and CMOS: a comparative view," Nucl. Instrum. Methods Phys. Res. A **504**, 199–212 (2003).
24. Hamamatsu, "CMOS linear image sensor s9226," Technical Application Note **KMPD1073E04** (2004).
25. Micron Technology, Inc., "2-megapixel low-power, CMOS image sensor," http://www.micron.com/products/imaging/products/MT9D011.html (2005).
26. K. Dennis, "Separation of mass uptake using two polar polymers for selective chemical detection," M.S. thesis (Georgia Institute of Technology, 2005).